

Current injection by coherent one- and two-photon excitation in graphene and its bilayerJ. Rioux,¹ Guido Burkard,² and J. E. Sipe¹¹*Department of Physics and Institute for Optical Sciences, University of Toronto, 60 St. George Street, Toronto, Ontario, Canada M5S 1A7*²*Department of Physics, University of Konstanz, D-78457 Konstanz, Germany*

(Received 20 January 2011; revised manuscript received 2 March 2011; published 3 May 2011)

Coherent control of optically injected carrier distributions in single and bilayer graphene allows the injection of electrical currents. Using a tight-binding model and Fermi's golden rule, we derive the carrier and photocurrent densities achieved via interference of the quantum amplitudes for two-photon absorption at a fundamental frequency, ω , and one-photon absorption at the second harmonic, 2ω . Strong currents are injected under co-circular and linear polarizations. In contrast, opposite-circular polarization yields no net current. For single-layer graphene, the magnitude of the current is unaffected by the rotation of linear-polarization axes, in contrast with the bilayer and with conventional semiconductors. The dependence of the photocurrent on the linear-polarization axes is a clear and measurable signature of interlayer coupling in AB-stacked multilayer graphene. We also find that single and bilayer graphene exhibit a strong, distinct linear-circular dichroism in two-photon absorption.

DOI: [10.1103/PhysRevB.83.195406](https://doi.org/10.1103/PhysRevB.83.195406)

PACS number(s): 73.50.Pz, 78.67.Wj, 42.65.-k

I. INTRODUCTION

The successful isolation of a single graphene sheet^{1,2} has sparked an intense research area around its unusual electronic and optical properties. Carriers in graphene obey Dirac's equation, resulting in an electronic energy-momentum dispersion that is linear, with intersecting electron and hole bands.³⁻⁵ At optical frequencies, the absorption per layer through a graphene stack is quantized in an amount written in terms of universal constants.⁶

Bilayer graphene has also garnered significant interest due to its quite different but equivalently interesting electronic properties. The carriers in clean, unbiased bilayer graphene obey a massive Dirac equation; their band dispersion is gapless, quadratic at low energy, and linear at high energy.^{7,8}

Both single and bilayer graphene are characterized by carrier mobilities that are extremely high.^{1,9} Their high optical conductivity and high carrier mobilities mean they could see applications as optically controlled transport devices.

For a level system subjected to coherent irradiation at a fundamental frequency and its ℓ th harmonic, the quantum interference of one- and ℓ -photon absorption pathways allows the coherent control (CC) of the excitation process. This quantum interference control technique has been widely used to study systems ranging from molecules to bulk and quantum well materials.¹⁰ For crystalline materials, where initial and final states are described by Bloch states, an often-studied method is the use of fundamental and second-harmonic frequencies. The two equivalent pathways consist of two-photon absorption of the fundamental and one-photon absorption of the second harmonic. The cross term of the transition amplitudes contributes to an asymmetrical distribution of injected carriers through reciprocal space, yielding a nonzero current density. The k -space distribution is controlled by attributes of the two coherent components of the light field: their polarization and a relative phase parameter.¹¹ In graphene, the interference effect for linearly polarized light has been predicted to be significantly stronger than in conventional semiconductors.¹² Photocurrent CC has been demonstrated experimentally in multilayer epitaxial graphene,¹³ carbon nanotubes, and graphite.¹⁴

In this paper, the tight-binding model of graphene near the Dirac point is used to calculate the distributions of carriers optically injected by simultaneous irradiation with light at a frequency ω and light at its second harmonic frequency 2ω . We find that the coherent adjustment of phase parameters and polarizations yield a photocurrent for linearly and co-circularly polarized light. The results for one and two layers of graphene are contrasted, and we argue that interlayer coupling could be probed in a Bernal stack of graphene sheets.

The paper is organized as follows. The effective Hamiltonians used for the calculations are presented in Sec. II. One- and two-photon absorption coefficients in single-layer graphene, the resulting distributions of injected carriers, and the generated photocurrents due to interference are presented in Sec. III; these results hold as well for the low-energy expansion of bilayer graphene. The full treatment of the bilayer and the effects of interlayer coupling on two-photon absorption and photocurrent injection are presented in Sec. IV. We summarize and discuss our results in Sec. V.

II. HAMILTONIANS

Single-layer graphene (henceforth simply graphene) is a one-atom-thick layer of carbon atoms arranged in two triangular sublattices {A, B}, as shown in Fig. 1(a). In the basis of the sublattices, the tight-binding model is expanded near the K point to yield the effective Hamiltonian

$$H_1(\mathbf{K} + \mathbf{k}) \rightarrow \hbar v_F \boldsymbol{\sigma} \cdot \mathbf{k} = v_F \begin{pmatrix} 0 & \hbar k_- \\ \hbar k_+ & 0 \end{pmatrix}, \quad (1)$$

where v_F is the Fermi velocity, $\boldsymbol{\sigma}$ are the Pauli matrices, \mathbf{k} is the crystal momentum in the plane of the crystal relative to the K point and $k_{\pm} = k_x \pm ik_y$. The Fermi velocity can be expressed in terms of the sublattice hopping term γ_0 .⁵ The resulting band energies are linear in crystal momentum k and are shown in Fig. 2.

The structure of Bernal-stacked bilayer graphene is sketched in Fig. 1(b); there are four atoms per unit cell, each contributing a p_z orbital to the π bands.¹⁵ The corresponding

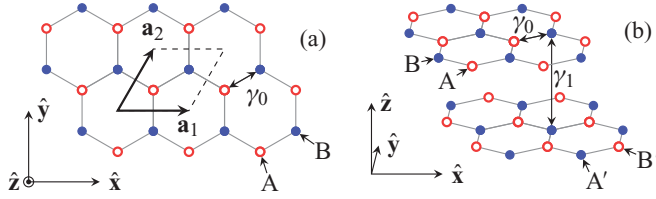


FIG. 1. (Color online) Crystal structure of (a) single-layer graphene and (b) bilayer graphene. The basis vectors \mathbf{a}_1 and \mathbf{a}_2 define the unit cell, γ_0 and γ_1 are the intralayer and interlayer coupling strengths, and the sublattices are denoted by A (A') and B (B').

4×4 tight-binding Hamiltonian, written in the basis $\{A, B', A', B\}$ and expanded near the K point, is given by

$$H_2(\mathbf{K} + \mathbf{k}) \rightarrow \begin{pmatrix} 0 & 0 & 0 & v_F \hbar k_- \\ 0 & 0 & v_F \hbar k_+ & 0 \\ 0 & v_F \hbar k_- & 0 & \gamma_1 \\ v_F \hbar k_+ & 0 & \gamma_1 & 0 \end{pmatrix}. \quad (2)$$

This tight-binding model includes γ_0 , the intralayer coupling, and γ_1 , the hopping term between sublattices A' and B from the two different layers. A low-energy expansion yields

$$H'_2(\mathbf{K} + \mathbf{k}) \rightarrow -\frac{\hbar^2}{2m} \begin{pmatrix} 0 & k_-^2 \\ k_+^2 & 0 \end{pmatrix}, \quad (3)$$

where $m = \gamma_1/2v_F^2$. This is the ‘‘massive’’ Dirac equation, describing the carriers near the K point for $|v_F \hbar k| \ll \gamma_1$. The energy dispersion consists of a pair of gapless conduction and valence bands touching at the Dirac point ($\mathbf{k} = 0$), with a quadratic dependence on crystal momentum.^{4,5}

Near the K' point, similar Hamiltonians are obtained by letting $k_x \rightarrow -k_x$ in Eqs. (1)–(3); for the purposes of this paper, the two valleys are equivalent.

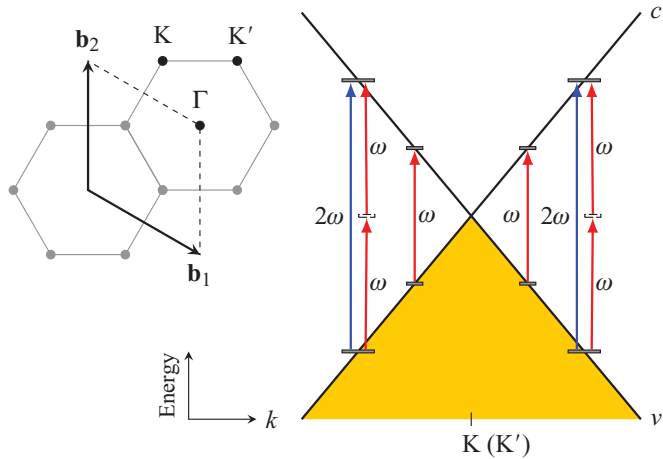


FIG. 2. (Color online) Reciprocal space and linear energy-crystal momentum dispersion of graphene near K . The basis vectors \mathbf{b}_1 and \mathbf{b}_2 form the reciprocal unit cell, enclosing one K and one K' valley. The dispersion shows the initially empty conduction band c and occupied valence band v touching at the K point. The excitation scheme employs interference between two-photon absorption at ω (red arrows) and one-photon absorption at 2ω (blue arrows), leading to generation of charge and current.

III. SINGLE-LAYER GRAPHENE

In this section, we use Eq. (1) to calculate one- and two-photon absorption coefficients, and the CC of chiral carriers in graphene. The velocity operator $\mathbf{v} = \frac{1}{\hbar} \nabla_{\mathbf{k}} H$, when written in the eigenstates basis, takes the form

$$\mathbf{v} \rightarrow v_F \begin{pmatrix} \hat{k} & i\hat{\phi} \\ -i\hat{\phi} & -\hat{k} \end{pmatrix}, \quad (4)$$

where \hat{k} is the unit vector parallel to the direction of \mathbf{k} and $\hat{\phi} = \hat{z} \times \hat{k}$.

A. Carrier injection

We calculate the rate of change of the carrier density due to an interaction Hamiltonian $H_{\text{int}} = -\frac{e}{m_0 c} \mathbf{A} \cdot \mathbf{p}$, where \mathbf{A} is the vector potential of the optical field, m_0 is the free-electron mass, c is the speed of light in vacuum, and $e = -|e|$ is the electron charge, by performing a perturbation calculation up to second order. Assuming a monochromatic field of frequency ω , we obtain expressions for the rate of injection of carrier density due to one- and two-photon absorption processes (using the Gaussian system of quantities and cgs units throughout):

$$\dot{n}_1 = \xi_1^{ab}(\omega) E^{a*}(\omega) E^b(\omega), \quad (5)$$

$$\dot{n}_2 = \xi_2^{abcd}(\omega) E^{a*}(\omega) E^{b*}(\omega) E^c(\omega) E^d(\omega), \quad (6)$$

where \mathbf{E} is the electric field and superscripts $a, b, c,$ and d indicate Cartesian components; repeated superscripts are summed over. Microscopic expressions for the tensors ξ_1 and ξ_2 are derived in the independent-particle approximation following Fermi's golden rule (FGR).^{11,16} For a two-dimensional crystal, we have

$$\dot{n}_\ell = 2\pi \sum_{c,v} \int \frac{d^2 k}{4\pi^2} |\Omega_{cv}^{(\ell)}(\omega, \mathbf{k})|^2 \delta[\omega_{cv}(\mathbf{k}) - \ell\omega], \quad (7)$$

where $\omega_{cv}(\mathbf{k}) \equiv \omega_c(\mathbf{k}) - \omega_v(\mathbf{k})$, $\hbar\omega_m(\mathbf{k})$ are the band energies, and $\Omega_{cv}^{(\ell)}(\omega, \mathbf{k})$ is the ℓ -photon transition amplitude between valence band v and conduction band c at wave vector \mathbf{k} ¹⁶:

$$\Omega_{cv}^{(1)}(\omega, \mathbf{k}) = \frac{ie}{\hbar\omega} \mathbf{v}_{cv}(\mathbf{k}) \cdot \mathbf{E}(\omega), \quad (8)$$

$$\Omega_{cv}^{(2)}(\omega, \mathbf{k}) = \frac{2e^2}{\hbar^2 \omega^2} \sum_m \frac{\mathbf{v}_{cm}(\mathbf{k}) \cdot \mathbf{E}(\omega) \mathbf{v}_{mv}(\mathbf{k}) \cdot \mathbf{E}(\omega)}{\omega_{mc}(\mathbf{k}) + \omega_{mv}(\mathbf{k})}, \quad (9)$$

where $\mathbf{v}_{mn}(\mathbf{k})$ indicate matrix elements of the velocity operator, and $[\omega_{mc}(\mathbf{k}) + \omega_{mv}(\mathbf{k})]/2 = \omega_m(\mathbf{k}) - [\omega_v(\mathbf{k}) + \omega]$ is the usual energy denominator appearing in second-order perturbation theory.

By the symmetry of graphene and bilayer graphene, the tensors ξ_1 and ξ_2 have respectively one and three nonzero independent components in the xy plane: ξ_1^{xx} , ξ_2^{xxxx} , ξ_2^{xyxy} , and $\xi_2^{xyyx} = \xi_2^{xyyx}$; however, all our model Hamiltonians are isotropic, reducing ξ_2 to two independent terms: ξ_2^{xxxx} and the linear-circular dichroism $\delta = \xi_2^{xyxy}/\xi_2^{xxxx}$.¹⁷

The electric field $\mathbf{E}(\omega)$ in an arbitrary beam at normal incidence can be written as $\mathbf{E}(\omega) = E_\omega e^{i\varphi_\omega} (\hat{\mathbf{x}}_\omega + \hat{\mathbf{y}}_\omega e^{i\delta\varphi_\omega})/\sqrt{2}$, for an appropriate choice of orthonormal vectors $\hat{\mathbf{x}}_\omega$ and $\hat{\mathbf{y}}_\omega$ in the xy plane, a real amplitude E_ω , and real phase parameters

φ_ω and $\delta\varphi_\omega$. The injection rates of the carrier density due to one- and two-photon processes are given by

$$\dot{n}_1 = \xi_1^{xx}(\omega) |E_\omega|^2, \quad (10)$$

$$\dot{n}_2 = \xi_2^{xxxx}(\omega) |E_\omega|^4 [1 - \delta \sin^2(\delta\varphi_\omega)]. \quad (11)$$

Both are insensitive to rotation of the crystal axes with respect to the normal, but one-photon absorption is independent of polarization, while two-photon absorption depends on the phase difference $\delta\varphi_\omega$ between the linearly polarized components of the incident light.

For the linear response, we find from Eq. (1) that $\xi_1^{xx} \equiv \bar{\xi}_1$, with

$$\bar{\xi}_1(\omega) = 2\sigma_0/\hbar\omega, \quad (12)$$

where σ_0 is the universal optical conductivity of graphene: $\sigma_0 = g_s g_v \frac{e^2}{16\hbar}$, with $g_s = 2$ and $g_v = 2$ denoting spin and valley degeneracy, respectively.^{6,18} For the two-photon process we find $\xi_2^{xxxx} = \xi_2^{xyxy} = \xi_2^{xyyx} = -\xi_2^{xyyx} \equiv \bar{\xi}_2$, with

$$\bar{\xi}_2(\omega) = 8g_s g_v \hbar e^4 v_F^2 (2\hbar\omega)^{-5}. \quad (13)$$

Thus, for chiral carriers, $\delta = -1$ and it follows from Eq. (11) that circularly polarized light ($\delta\varphi_\omega = \pm\frac{\pi}{2}$) provides twice as much two-photon absorption as linearly polarized light.

B. Quantum interference of fundamental and second harmonic components

In the presence of a two-color optical field with frequency components ω and 2ω , there exist two transition amplitudes connecting the same initial and final states: $\Omega_{cv}^{(1)}(2\omega, \mathbf{k})$ results from light at 2ω to first order in perturbation, and $\Omega_{cv}^{(2)}(\omega, \mathbf{k})$ results from light at ω to second order in perturbation. The cross term of these amplitudes yields the CC term. Although this has no effect on the total number of carriers optically injected in centrosymmetric crystals,¹⁹ it yields an injection term for the current density. This term has the form

$$\mathbf{j}^a = \eta_I^{abcd}(\omega) E^{b*}(\omega) E^{c*}(\omega) E^d(2\omega) + \text{c.c.}, \quad (14)$$

where $\eta_I(\omega)$ is a fourth-rank current-injection tensor.¹¹ The symmetry of graphene or bilayer graphene yields η_I^{xxxx} , η_I^{xyyx} , and $\eta_I^{xyxy} = \eta_I^{xyyx}$ as independent components; an isotropic model has $2\eta_I^{xyxy} = \eta_I^{xxxx} - \eta_I^{xyyx}$.^{20,21} We introduce a disparity parameter $d = \eta_I^{xyyx}/\eta_I^{xxxx}$ to characterize how the current injection due to linearly polarized beams depends on whether the polarization axes are perpendicular or parallel:

$$\mathbf{J} = \eta_I^{xxxx}(\omega) [\mathbf{E}^*(\omega) [\mathbf{E}^*(\omega) \cdot \mathbf{E}(2\omega)] - d \mathbf{E}^*(\omega) \times [\mathbf{E}^*(\omega) \times \mathbf{E}(2\omega)]] + \text{c.c.} \quad (15)$$

From Eq. (1) we find that the nonzero components of the current-injection tensor are related by $\eta_I^{xxxx} = \eta_I^{xyxy} = \eta_I^{xyyx} = -\eta_I^{xyyx} \equiv i\bar{\eta}_I$, and thus $d = -1$. In the independent-particle approximation, $\bar{\eta}_I$ is purely real. An FGR derivation predicts equal conduction- and valence-band contributions, for a total current injection

$$\bar{\eta}_I(\omega) = g_s g_v e^4 v_F^2 (2\hbar\omega)^{-3}. \quad (16)$$

We describe ω and 2ω beams at normal incidence by the choice of fields $\mathbf{E}(\omega) = E_\omega e^{i\varphi_\omega} \hat{\mathbf{e}}_\omega$ and $\mathbf{E}(2\omega) = E_{2\omega} e^{i\varphi_{2\omega}} \hat{\mathbf{e}}_{2\omega}$,

where $\hat{\mathbf{e}}_{\omega/2\omega} = (\hat{\mathbf{x}}_{\omega/2\omega} + \hat{\mathbf{y}}_{\omega/2\omega} e^{i\delta\varphi_{\omega/2\omega}})/\sqrt{2}$, describing two arbitrary normal-incidence beams. We find that co-circularly polarized beams ($\delta\varphi_\omega = \delta\varphi_{2\omega} = \pm\frac{\pi}{2}$) yield the current injection with the largest magnitude:

$$\mathbf{J} = 2\sqrt{2}\bar{\eta}_I(\omega) E_\omega^2 E_{2\omega} \hat{\mathbf{m}}, \quad (17)$$

where $\hat{\mathbf{m}} = \hat{\mathbf{x}}_{2\omega} \sin(\Delta\varphi \mp 2\theta) \pm \hat{\mathbf{y}}_{2\omega} \cos(\Delta\varphi \mp 2\theta)$. The phase-difference parameter $\Delta\varphi \equiv 2\varphi_\omega - \varphi_{2\omega}$ controls the direction of the current; θ is the angle that separates the polarization axes of the fundamental from those of the second harmonic: $\hat{\mathbf{x}}_\omega = \hat{\mathbf{x}}_{2\omega} \cos\theta + \hat{\mathbf{y}}_{2\omega} \sin\theta$. Opposite-circular polarizations ($-\delta\varphi_\omega = \delta\varphi_{2\omega} = \pm\frac{\pi}{2}$) yield no net current injection, while linearly polarized beams ($\delta\varphi_\omega = \delta\varphi_{2\omega} = 0$) yield

$$\mathbf{J} = 2\bar{\eta}_I(\omega) E_\omega^2 E_{2\omega} \sin(\Delta\varphi) \hat{\mathbf{n}}, \quad (18)$$

where $\hat{\mathbf{n}} = \hat{\mathbf{e}}_{2\omega} \cos(2\theta) + \hat{\mathbf{e}}_{2\omega}^\perp \sin(2\theta)$ and $\hat{\mathbf{e}}_{2\omega}^\perp = \hat{\mathbf{z}} \times \hat{\mathbf{e}}_{2\omega}$. Here the angle θ between polarization axes controls the orientation of the current within the graphene plane, and $\Delta\varphi$ controls its magnitude. For co-linearly polarized and cross-polarized beams, the injected current is parallel with the direction of $\hat{\mathbf{e}}_{2\omega}$, the polarization axis of the second harmonic. Conversely the injected current is perpendicular to $\hat{\mathbf{e}}_{2\omega}$ when the polarization axes form an angle of $\theta = \frac{\pi}{4}$. Within this model, the orientation of the crystal axes has no influence on the current injection at normal incidence.

Graphene seems to be the first material that has been studied for which any value of θ is equally effective at injecting a current. This is in contrast to materials such as GaAs, where one finds $|\eta_I^{xyyx}| \ll |\eta_I^{xxxx}|$, and thus a configuration with perpendicular polarization axes results in a significantly weaker current.^{11,20,21}

Figure 3 shows the k -space distribution of the carrier-injection rate, $\dot{n}(\mathbf{k}) = |\Omega_{cv}^{(1)}(2\omega, \mathbf{k}) + \Omega_{cv}^{(2)}(\omega, \mathbf{k})|^2$, at $\omega_{cv}(\mathbf{k}) = 2\omega$. Field amplitudes are chosen such that the integrated injection rates from one- and two-photon processes are balanced: $\dot{n}_1(2\omega) = \dot{n}_2(\omega)$. Opposite-circular polarization of the beams yields the nonpolar distribution in Fig. 3(a) and no net current. In Fig. 3(b) both components of the two-color field have the same circular polarization σ^\pm . The carrier distribution follows $\dot{n}(\mathbf{k}) \propto 1 + \sin(\Delta\varphi \pm \phi_k)$, where $\phi_k = \tan^{-1}(k_y/k_x)$, resulting in the injection of the current given by Eq. (17). The charge distribution and current rotate with $\Delta\varphi$: clockwise for σ^+ and counterclockwise for σ^- , when viewed from $z > 0$.

In Figs. 3(c) and 3(d) we show the k -space distribution of the carrier-injection rate for linearly polarized light; without loss of generality, $\hat{\mathbf{e}}_{2\omega}$ is taken along the x axis: $\hat{\mathbf{e}}_{2\omega} = \hat{\mathbf{x}}$ and $\hat{\mathbf{e}}_\omega = \hat{\mathbf{x}} \cos\theta + \hat{\mathbf{y}} \sin\theta$. Taking the phase-difference parameter to be $\Delta\varphi = \frac{\pi}{2}$, we maximize both the cross term in the k -dependent carrier density, $\dot{n}(\mathbf{k}) \propto |\sin\phi_k + i e^{-i\Delta\varphi} \sin(2\phi_k - 2\theta)|^2$, and the resulting current, Eq. (18). For co-linear polarization axes as in Fig. 3(c), the distribution is symmetric with respect to k_y , while asymmetric and strongly enhanced toward positive k_x , although with a node at $\phi_k = 0$. The excess of positive- k_x carriers gives rise to a net electric current along the x axis. As the polarization axis of the ω component is rotated by the angle θ , carriers are redistributed toward positive k_y . At $\theta = \frac{\pi}{4}$, $\dot{n}(\mathbf{k})$ is symmetric with respect to k_x and the net current is along the y axis [Fig. 3(d)].

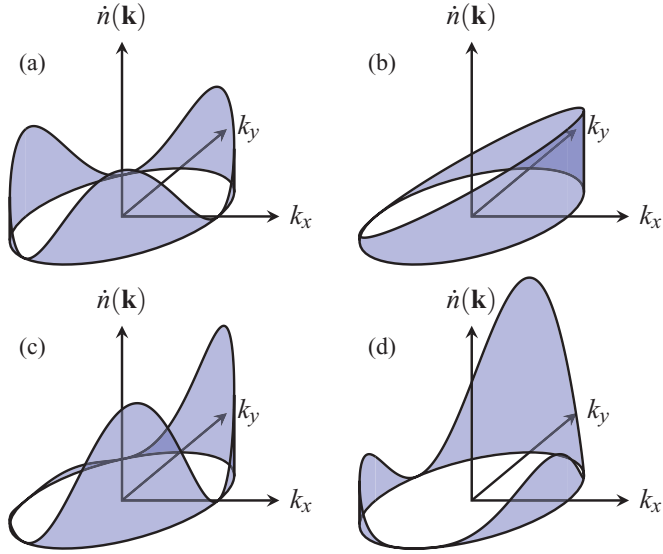


FIG. 3. (Color online) Distribution $\dot{n}(\mathbf{k})$ of the carrier injection through reciprocal space under irradiation by an optical field with components $E(\omega)$ and $E(2\omega)$ satisfying $\Delta\varphi = \frac{\pi}{2}$. (a) Opposite-circular polarization ($-\delta\varphi_\omega = \delta\varphi_{2\omega} = \pm\frac{\pi}{2}, \theta = 0$). (b) Co-circular polarization (σ^\pm light, $\delta\varphi_\omega = \delta\varphi_{2\omega} = \pm\frac{\pi}{2}, \theta = 0$). (c), (d) Linear polarization ($\delta\varphi_\omega = \delta\varphi_{2\omega} = 0$) with $\hat{\mathbf{e}}_{2\omega} = \hat{\mathbf{x}}$ and $\hat{\mathbf{e}}_\omega = \hat{\mathbf{x}} \cos \theta + \hat{\mathbf{y}} \sin \theta$; (c) $\theta = 0$ and (d) $\theta = \frac{\pi}{4}$. The distribution in (a) results in no net current; the asymmetric distributions [(b)–(d)] result in net electrical currents injected in the graphene plane along $\hat{\mathbf{x}}$ [(b), (c)] or $\hat{\mathbf{y}}$ (d).

IV. BILAYER GRAPHENE

The chiral Hamiltonian for bilayer graphene, Eq. (3), results in the same carrier and current injection as in the previous section if we replace $\xi_1 \rightarrow 2\xi_1$, $\xi_2 \rightarrow 8\hbar\omega\xi_2/\gamma_1$, and $\eta_I \rightarrow 8\hbar\omega\eta_I/\gamma_1$; the velocity operator in the eigenstates basis takes the form of Eq. (4) with $v_F \rightarrow \hbar k/m$, and thus the symmetry properties of the injection tensors are unchanged. But such a treatment describes the carriers only near the K point for $|v_F\hbar k| \ll \gamma_1$ and leaves out important remote bands in the two-photon transition amplitude. A more accurate model is given by Eq. (2), which is also valid for band energies on the order of γ_1 . This 4×4 Hamiltonian introduces two additional bands, one above and one below the Dirac point, shifted by an energy γ_1 . More importantly, it gives the correct linear dispersion for larger values of k . The band dispersion near K is shown in Fig. 4.

A. Carrier injection

Starting from Eq. (2), in this section we repeat the previous injection-tensor calculations for the unbiased Bernal-stacked graphene bilayer. The one-photon carrier injection of bilayer graphene is obtained from Eq. (12) by replacing σ_0 with the bilayer optical conductivity σ from Abergel and Fal'ko.²²

We break down the two-photon carrier injection into four distinct contributions. The first (a) comes from absorption by the gapless doublet (leftmost transition in Fig. 4, denoted GLT). The second and third contributions arise from injection involving exactly one split-off band and contain either (b) only two-band or three-band amplitudes and no cross term,

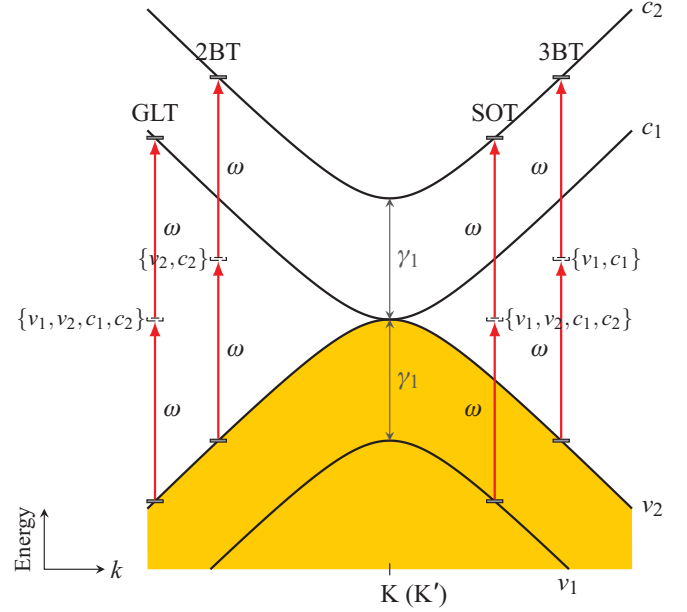


FIG. 4. (Color online) Band dispersion of bilayer graphene and breakdown of the transition amplitudes for two-photon absorption. Bands v_1 and v_2 are valence bands and initially filled; c_1 and c_2 are initially empty conduction bands. Bands v_2 and c_1 form a gapless doublet touching at the K point; c_2 and v_1 are split-off bands shifted by an energy γ_1 above and below the gapless doublet, respectively. All bands are quadratic near K and linear at larger k . Transition amplitudes appear in four variants: (i) the gapless term (GLT) between bands v_2 and c_1 , (ii) two- and (iii) three-band terms involving exactly one split-off band (2BT and 3BT, respectively), and (iv) the split-off term (SOT) between bands v_1 and c_2 . The notation $\{\dots\}$ next to a virtual state indicates that the sum in Eq. (9) is restricted to $m \in \{\dots\}$. Not shown are the 2BT and 3BT between bands v_1 and c_1 .

or (c) cross terms of two- and three-band amplitudes; two- and three-band amplitudes are denoted 2BT and 3BT in Fig. 4. The fourth contribution (d) comes from absorption where initial and final states are split-off bands (SOT in Fig. 4). The nonzero tensor components are obtained from the symmetry of the matrix elements involved for each contribution, which yields

$$\xi_2^{xxxx}(\omega) = \bar{\xi}_{2a}(\omega) + [3\bar{\xi}_{2b}(\omega) + \bar{\xi}_{2c}(\omega)] \Theta(2\hbar\omega - \gamma_1) + \bar{\xi}_{2d}(\omega) \Theta(2\hbar\omega - 2\gamma_1), \quad (19a)$$

$$\xi_2^{xyyy}(\omega) = -\bar{\xi}_{2a}(\omega) + [\bar{\xi}_{2b}(\omega) + 3\bar{\xi}_{2c}(\omega)] \Theta(2\hbar\omega - \gamma_1) - \bar{\xi}_{2d}(\omega) \Theta(2\hbar\omega - 2\gamma_1), \quad (19b)$$

where $\Theta(x)$ is the Heaviside step function. The matrix elements appearing in $\bar{\xi}_{2a}$ and $\bar{\xi}_{2d}$ have the same symmetry as those appearing in graphene. However, the contributions involving exactly one split-off band (b, c) break the graphene result of $\delta = -1$. Indeed, if one defines a partial linear-circular dichroism $\delta_i = \bar{\xi}_{2i}^{xyyy}/\bar{\xi}_{2i}^{xxxx}$ for each contribution $i \in \{a, b, c, d\}$, it follows that $\delta_a = -1$, $\delta_b = \frac{1}{3}$, $\delta_c = 3$, and $\delta_d = -1$. The total linear-circular dichroism will depend on the relative strength of the contributions $\bar{\xi}_{2a-d}$, which we now address.

In computing $\Omega_{cv}^{(2)}(\omega, \mathbf{k})$ for the bilayer, a difficulty arises since it is possible for the energy denominator inside the sum in Eq. (9) to become exactly zero. Take for example the top valence band as initial state v and the second conduction band as final state c . When the intermediate state m is the first conduction band, there exists a value of k such that $\hbar\omega_m(\mathbf{k}) = \frac{1}{2}\gamma_1$; at this k the intermediate state lies precisely in between the initial and final states. This leads to a resonance in the calculated response functions at $\hbar\omega = \gamma_1$. To avoid this resonance, we let $\omega_m \rightarrow \omega_m + i\Gamma/2\hbar$ in Eq. (9). The linewidth Γ accounts phenomenologically for dephasing due to actual population of the intermediate state. Other linewidths could be added to describe the effects of disorder or interactions, but for values $\lesssim \Gamma$ we find that their inclusion does not significantly modify our results.

With $\bar{\xi}_2(\omega)$ given in Eq. (13), we have

$$\bar{\xi}_{2a}(\omega) = \bar{\xi}_2(\omega) \frac{2\hbar\omega(2\hbar\omega + 3\gamma_1)^2}{(2\hbar\omega + \gamma_1)(2\hbar\omega + 2\gamma_1)^2}, \quad (20a)$$

$$\begin{aligned} \bar{\xi}_{2b}(\omega) = \bar{\xi}_2(\omega) \frac{2\gamma_1^2(2\hbar\omega + \gamma_1)(2\hbar\omega - \gamma_1)}{(2\hbar\omega)^2(2\hbar\omega + 2\gamma_1)^2} \\ \times \left(\frac{(2\hbar\omega + 2\gamma_1)^2}{(2\hbar\omega)^2} + \frac{(2\hbar\omega)^2 + \frac{1}{4}\Gamma^2}{(2\hbar\omega - 2\gamma_1)^2 + \Gamma^2} \right), \end{aligned} \quad (20b)$$

$$\begin{aligned} \bar{\xi}_{2c}(\omega) = -\bar{\xi}_2(\omega) \frac{2\gamma_1^2}{(2\hbar\omega)^3} (2\hbar\omega + \gamma_1)(2\hbar\omega - \gamma_1) \\ \times \left(\frac{1}{2\hbar\omega + 2\gamma_1} + \frac{2\hbar\omega - 2\gamma_1}{(2\hbar\omega - 2\gamma_1)^2 + \Gamma^2} \right), \end{aligned} \quad (20c)$$

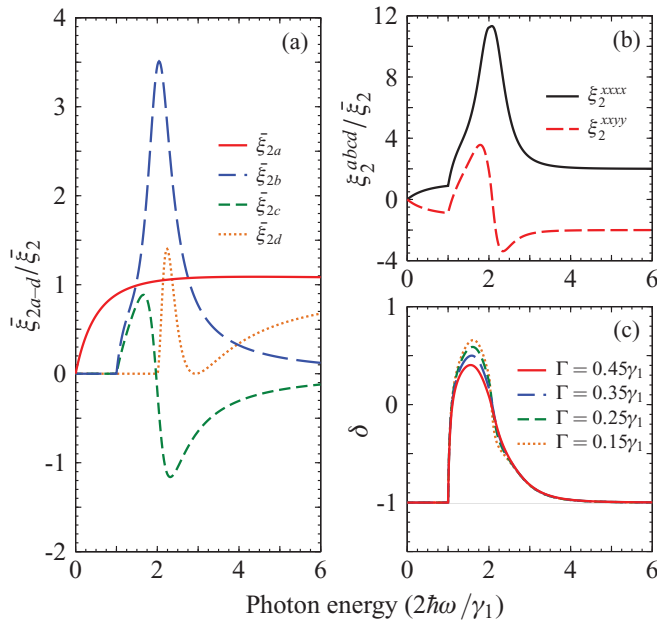


FIG. 5. (Color online) Quantities describing two-photon carrier injection in bilayer graphene as a function of photon energy for an intermediate-state linewidth $\Gamma/\gamma_1 = 0.35$. (a) The individual contributions $\bar{\xi}_{2a-d}$ (a , plain red; b , long-dashed blue; c , short-dashed green; d , dotted orange) from Eq. (20). (b) The independent nonzero tensor components $\bar{\xi}_2^{xxxx}$ (plain black) and $\bar{\xi}_2^{xyxy}$ (dashed red) from Eq. (19). (c) The linear-circular dichroism $\delta = \bar{\xi}_2^{xyyx}/\bar{\xi}_2^{xxxx}$.

$$\begin{aligned} \bar{\xi}_{2d}(\omega) = \bar{\xi}_2(\omega) \frac{2\hbar\omega(2\hbar\omega - 2\gamma_1)^2}{(2\hbar\omega - \gamma_1)^3} \\ \times \left(1 - \frac{\gamma_1^2}{(2\hbar\omega - 2\gamma_1)^2 + \Gamma^2} \right). \end{aligned} \quad (20d)$$

We graph the individual contributions $\bar{\xi}_{2a-d}$ in Fig. 5(a) and the resulting $\bar{\xi}_2^{xxxx}$ and $\bar{\xi}_2^{xyxy}$ components of the two-photon carrier-injection tensor in Fig. 5(b). In contrast to the linear absorption, where the limits of the bilayer response function at low and high photon energies gave the graphene result times a factor of 2,²² in the two-photon response function this “factor of 2” rule does not hold at low photon energy: For $\hbar\omega \ll \gamma_1$, we find $\bar{\xi}_{2(\text{bilayer})}^{abcd}(\omega) \rightarrow 9\hbar\omega \bar{\xi}_{2(\text{graphene})}^{abcd}(\omega)/2\gamma_1$. Further, using Eq. (3) instead yields $\bar{\xi}_{2(\text{bilayer})}^{abcd}(\omega) \rightarrow 8\hbar\omega \bar{\xi}_{2(\text{graphene})}^{abcd}(\omega)/\gamma_1$; the discrepancy is explained since the derivation using the 4×4 Hamiltonian includes important three-band terms from the split-off bands in the two-photon transition amplitude. At high photon energy $\bar{\xi}_{2(\text{bilayer})}^{abcd}(\omega) \rightarrow 2\bar{\xi}_{2(\text{graphene})}^{abcd}(\omega)$ as expected.

Two features are apparent in the response tensor at the thresholds for absorption into the split-off bands. The first feature is a pronounced shoulder in both $\bar{\xi}_2^{xxxx}$ and $\bar{\xi}_2^{xyxy}$ at $2\hbar\omega = \gamma_1$ due to the onset of absorption involving one split-off band. The second feature is the resonance which occurs at $2\hbar\omega = 2\gamma_1$. There the contributions $\bar{\xi}_{2b}$ and $\bar{\xi}_{2c}$ approximate the real and imaginary parts of a complex Lorentzian function, and contribute to a peak in $\bar{\xi}_2^{xxxx}$ and a change of sign in $\bar{\xi}_2^{xyxy}$.

In Figs. 5(a) and 5(b) we have chosen the particular value $\Gamma = 0.35\gamma_1$ for the linewidth. We note that $\bar{\xi}_{2a}$ is independent of Γ , but $\bar{\xi}_{2b-d}$ are not. However, the graph of these quantities changes quantitatively but not qualitatively when a different finite value is chosen for Γ . We plot the linear-circular dichroism δ in Fig. 5(c) for different values of Γ . It can be seen that Γ has very little effect on δ . The graphene result ($\delta = -1$) is reproduced for $2\hbar\omega < \gamma_1$ and $2\hbar\omega \gtrsim 3\gamma_1$. For mid-frequencies, $\gamma_1 < 2\hbar\omega < 2\gamma_1$, the dichroism increases (decreases) sharply at the first (second) split-off band threshold; δ changes sign and has a maximum value ~ 0.5 near $2\hbar\omega = 1.5\gamma_1$.

B. Current injection

There are four contributions to the current-injection tensor in bilayer graphene, outlined in Fig. 6: The first (a) comes from absorption by the gapless doublet. The second and third contributions arise from injection involving exactly one split-off band, with the second-order amplitude containing either (b) only two-band terms or (c) only three-band terms. Transitions involving only the split-off bands make up the fourth contribution (d). Each individual process involves matrix elements of varying symmetry, and they contribute differently to η_I^{xxxx} and η_I^{xyyx} : >

$$\begin{aligned} \eta_I^{xxxx}(\omega) = i\bar{\eta}_{Ia}(\omega) + [3i\bar{\eta}_{Ib}(\omega) + i\bar{\eta}_{Ic}(\omega)] \Theta(2\hbar\omega - \gamma_1) \\ + i\bar{\eta}_{Id}(\omega) \Theta(2\hbar\omega - 2\gamma_1), \end{aligned} \quad (21a)$$

$$\begin{aligned} \eta_I^{xyyx}(\omega) = -i\bar{\eta}_{Ia}(\omega) + [i\bar{\eta}_{Ib}(\omega) + 3i\bar{\eta}_{Ic}(\omega)] \Theta(2\hbar\omega - \gamma_1) \\ - i\bar{\eta}_{Id}(\omega) \Theta(2\hbar\omega - 2\gamma_1). \end{aligned} \quad (21b)$$

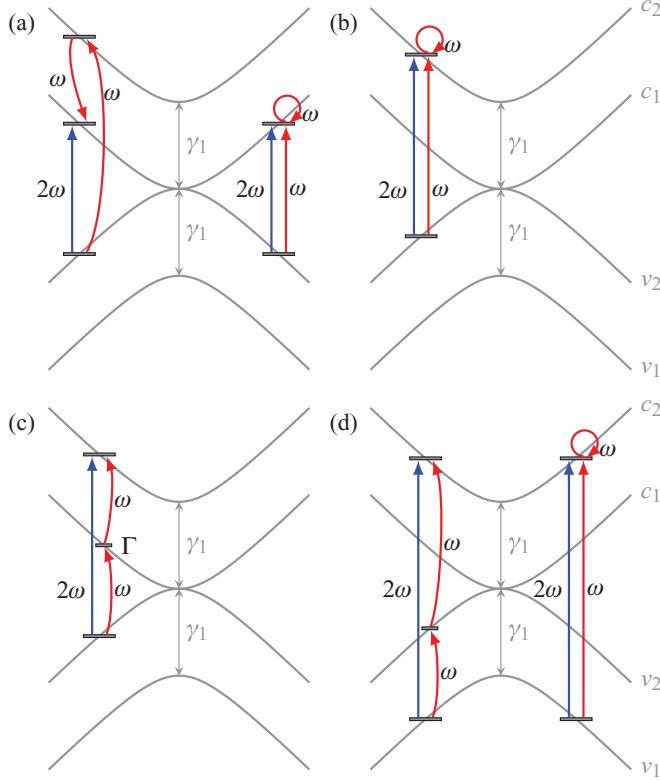


FIG. 6. (Color online) Diagrams of the four contributions $\bar{\eta}_{Ia-d}$ to the current injection in bilayer graphene [IV B].

The four contributions have dissimilar values of the parallel-perpendicular polarization disparity parameter: $d_a = -1$, $d_b = \frac{1}{3}$, $d_c = 3$, and $d_d = -1$. Their magnitudes are given by

$$\bar{\eta}_{Ia}(\omega) = \bar{\eta}_I(\omega) \frac{2\hbar\omega}{(2\hbar\omega + \gamma_1)^2} (2\hbar\omega + 3\gamma_1), \quad (22a)$$

$$\bar{\eta}_{Ib}(\omega) = \bar{\eta}_I(\omega) \frac{2\gamma_1^2}{(2\hbar\omega)^2} \frac{(2\hbar\omega + \gamma_1)(2\hbar\omega - \gamma_1)}{(2\hbar\omega)^2}, \quad (22b)$$

$$\begin{aligned} \bar{\eta}_{Ic}(\omega) &= -\bar{\eta}_I(\omega) \frac{\gamma_1^2 (2\hbar\omega + \gamma_1)(2\hbar\omega - \gamma_1)}{(2\hbar\omega)^3} \\ &\times \left(\frac{1}{2\hbar\omega + 2\gamma_1} + \frac{2\hbar\omega - 2\gamma_1}{(2\hbar\omega - 2\gamma_1)^2 + \Gamma^2} \right), \quad (22c) \end{aligned}$$

$$\begin{aligned} \bar{\eta}_{Id}(\omega) &= \bar{\eta}_I(\omega) \frac{2\hbar\omega}{(2\hbar\omega - \gamma_1)^3} (2\hbar\omega - 2\gamma_1)^2 \\ &\times \left(1 - \frac{\gamma_1^2}{(2\hbar\omega - 2\gamma_1)^2 + \Gamma^2} \right), \quad (22d) \end{aligned}$$

with $\bar{\eta}_I(\omega)$ given in Eq. (16). The parameters $\bar{\eta}_{Ia-d}$ are plotted in Fig. 7(a). The two independent components of η_I in the isotropic model, η_I^{xxxx} and η_I^{xyyx} , are plotted in Fig. 7(b). In the high-frequency limit, the current-injection tensor for the bilayer tends to $\eta_{I(\text{bilayer})}^{abcd}(\omega) \rightarrow 2\eta_{I(\text{graphene})}^{abcd}(\omega)$. In the low-frequency limit, we get $\eta_{I(\text{bilayer})}^{abcd}(\omega) \rightarrow 6\hbar\omega\eta_{I(\text{graphene})}^{abcd}(\omega)/\gamma_1$, in contrast to using the simple Hamiltonian of Eq. (3) which neglects three-band terms in the second-order ampli-

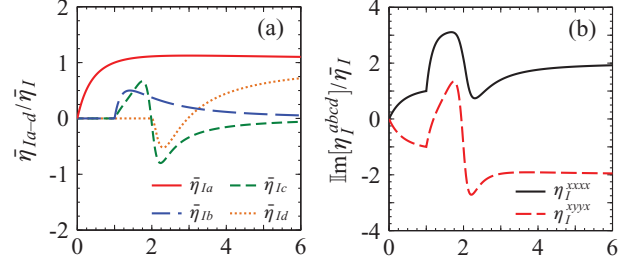


FIG. 7. (Color online) The current-injection tensor η_I in bilayer graphene for an intermediate-state linewidth $\Gamma/\gamma_1 = 0.25$. (a) The four contributions $\bar{\eta}_{Ia-d}$ from Eq. (22): Plain red, long-dashed blue, short-dashed green, and dotted orange curves correspond to components a , b , c , and d , respectively. (b) The tensor components η_I^{xxxx} (plain black) and η_I^{xyyx} (dashed red).

tude and gave $\eta_{I(\text{bilayer})}^{abcd}(\omega) \rightarrow 8\hbar\omega\eta_{I(\text{graphene})}^{abcd}(\omega)/\gamma_1$ (see the start of Sec. IV).

For mid-frequencies, there is a sharp increase in η_I at the first split-off band edge at $2\hbar\omega = \gamma_1$ and a sharp decrease at the second edge at $2\hbar\omega = 2\gamma_1$. Two features are manifest as a consequence of these split-off band edges: (i) In the region $\gamma_1 < 2\hbar\omega < 2\gamma_1$ the η_I^{xyyx} component changes sign. (ii) For $2\hbar\omega \gtrsim 2\gamma_1$ the η_I^{xxxx} component becomes very small.

The main difference between the current injection in graphene and in the bilayer is the contribution of components $\bar{\eta}_{Ib}$ and $\bar{\eta}_{Ic}$, each with a vastly different value of the disparity parameter: $d_b = \frac{1}{3}$ and $d_c = 3$ while in graphene $d = -1$. In Fig. 8 we plot the frequency dependence of d in bilayer graphene. The spectrum shows a constant -1 value from zero frequency until a sharp increase at the first split-off band edge at $2\hbar\omega = \gamma_1$; d rises with photon energy and eventually switches sign. At the second split-off band edge at $2\hbar\omega = 2\gamma_1$, d reverses sign abruptly; for the range $2\gamma_1 < 2\hbar\omega \lesssim 3\gamma_1$ it takes on large negative values as η_I^{xyyx} remains finite but η_I^{xxxx} becomes small [cf. Fig. 7(b)]. The value of d tends to -1 at higher photon energy.

We now consider current injection in bilayer graphene under irradiation by ω and 2ω beams at normal incidence. Choosing the electric fields $\mathbf{E}(\omega)$ and $\mathbf{E}(2\omega)$ as in the previous section, the current injection is given for co-circular polarization of the beams ($\delta\varphi_\omega = \delta\varphi_{2\omega} = \pm\frac{\pi}{2}$) by

$$\mathbf{J} = (1-d)\sqrt{2}\mathbb{I}m[\eta_I^{xxxx}]E_\omega^2E_{2\omega}\hat{\mathbf{m}} \quad (23)$$

and for opposite-circular polarization ($-\delta\varphi_\omega = \delta\varphi_{2\omega} = \pm\frac{\pi}{2}$) by $\mathbf{J} = 0$. In Eq. (23), the disparity parameter d only affects the magnitude of the current. In contrast, for linearly-polarized ω and 2ω beams ($\delta\varphi_\omega = \delta\varphi_{2\omega} = 0$) forming an angle θ between their polarization axes, different values of d lead to injected currents with different magnitudes but also with vastly dissimilar angular dependencies:

$$\begin{aligned} \mathbf{J} &= 2\mathbb{I}m[\eta_I^{xxxx}]E_\omega^2E_{2\omega}\sin(\Delta\varphi) \\ &\times \left[f(\theta, d)\hat{\mathbf{e}}_{2\omega} + g(\theta, d)\hat{\mathbf{e}}_{2\omega}^\perp \right], \quad (24) \end{aligned}$$

where $f(\theta, d) = \cos^2\theta + d\sin^2\theta$ and $g(\theta, d) = \frac{1}{2}(1-d)\sin 2\theta$. Thus, the current component that is parallel to

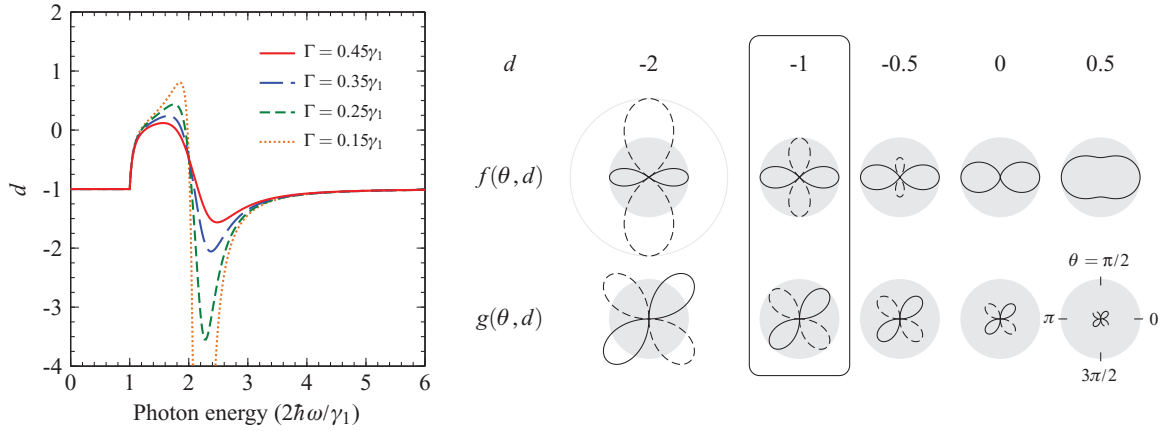


FIG. 8. (Color online) Results for the current injection in bilayer graphene with linearly polarized ω and 2ω beams. Left-hand side: The disparity parameter $d = \eta_I^{xyyx}/\eta_I^{xxxx}$ describing the asymmetry between parallel and perpendicular polarization axes, with $\Gamma/\gamma_1 = 0.15$ (dotted orange), 0.25 (short-dashed green), 0.35 (long-dashed blue), and 0.45 (plain red). Right-hand side: Polar plots of $f(\theta, d)$ and $g(\theta, d)$, the angular distributions of the projections of \mathbf{J} parallel and perpendicular to $\hat{\mathbf{e}}_{2\omega}$, as a function of the angle θ between the polarization vectors for $d = -2, -1, -0.5, 0$, and 0.5 . The shaded circles represent unit amplitude and dashed lines represent negative projections. The graphene prediction, $d = -1$, is highlighted.

$\hat{\mathbf{e}}_{2\omega}$ has a nonseparable dependence on θ and d , whereas the perpendicular component always follows $\sin 2\theta$. Polar plots of the functions $f(\theta, d)$ and $g(\theta, d)$ are shown on the right-hand side of Fig. 8 for $d = -2, -1, -0.5, 0$, and 0.5 . Our result for graphene ($d = -1$) yields a clover-shaped angular distribution: the $\cos 2\theta$ dependence in Eq. (18). For more (or less) negative values of d , the lobes around $\theta = \frac{\pi}{2}$ and $\frac{3\pi}{2}$ become more (or less) important. At $d = 0$, these two lobes vanish; any current injected with perpendicular ω and 2ω polarization axes is completely perpendicular to $\hat{\mathbf{e}}_{2\omega}$. For $d > 0$ there are no nodes in the angular distribution. For $|d| > 1$ the current parallel to $\hat{\mathbf{e}}_{2\omega}$ is stronger for perpendicular polarization axes compared to parallel polarization axes. By scanning the photon energy in the range $\gamma_1 < 2\hbar\omega \lesssim 3\gamma_1$, the disparity parameter d and thus the angular dependence of the current injection in bilayer graphene vary significantly, in contrast with the current injection in single-layer graphene. We note in particular that the sharp changes in the value of d near $2\hbar\omega \approx \gamma_1$ and $2\hbar\omega \approx 2\gamma_1$ should be perceived experimentally by rapid transitions in the angular dependence of the currents as the photon energy is scanned.

V. SUMMARY AND DISCUSSION

We have calculated the response tensors for one- and two-photon carrier injection and two-color current injection in graphene and bilayer graphene. We find a strong, frequency-independent linear-circular dichroism $\delta = -1$ in the two-photon response of graphene; for the bilayer, δ also equals -1 when $2\hbar\omega < \gamma_1$ or $2\hbar\omega \gtrsim 3\gamma_1$, and changes sign when $\gamma_1 < 2\hbar\omega \lesssim 3\gamma_1$. Using the optical CC technique, in-plane currents are generated for co-circularly polarized and linearly polarized beams. Such currents could be detected in experiments making use of contacts, or by detecting the emitted THz from the accelerated charges as was demonstrated by Sun *et al.* in epitaxially grown multilayer graphene.¹³ In the bilayer, the dependence on the angle θ between linearly polarized light

components at ω and 2ω is strongly sensitive to the photon energy for $\gamma_1 < 2\hbar\omega \lesssim 3\gamma_1$. This angular dependence is in sharp contrast to the prediction for a single graphene layer, and could be mapped out experimentally as a signature for interlayer coupling in epitaxially grown multilayer graphene samples, which are essentially thought of as uncoupled graphene layers.²³ We have assumed that the Fermi energy is at the Dirac point, but for a nonzero Fermi energy E_F , our predictions hold for $\hbar\omega > |E_F|$. When the Fermi energy varies across an inhomogeneous sample, E_F should be taken as the largest local Fermi energy.

Our description of the bilayer considers only the strongest of the interlayer coupling parameters, γ_1 , and excludes the next-to-nearest coupling parameters γ_3 and γ_4 . These terms break the isotropy of the model and introduce trigonal warping.⁵ However, we feel that excluding them in a first calculation is justified. The inclusion of γ_3 hardly changes the conductivity spectrum.²⁴ The same can be said of including the next-to-nearest neighbor hopping term in the Hamiltonian for graphene.²⁵

A natural extension of the current model is to consider AB-stacked multilayer graphene samples. Koshino and Ando have shown that for n layers with n even, the Hamiltonian can be decoupled into $n/2$ bilayers [with n odd, $(n-1)/2$ bilayers, and one decoupled single layer].²⁶ Each bilayer pair has a reduced coupling strength $\lambda_m \gamma_1$ where $\lambda_m = 2 \cos \kappa_m$ and κ_m is a wave vector in the stacking direction. The response of the multilayer system is the sum of the bilayer system's responses with detuned coupling strengths. In the limit of a high number of layers, the wave vector κ becomes a continuous variable and there is a continuous spectrum of resonances, smearing out the response tensor and eventually modeling the response of bulk graphite.

In the present paper, spin and valley degrees of freedom have contributed only degeneracy factors of 2 to the injection tensors. But spin- or valley-polarized currents could also be photogenerated if we first lifted the spin or valley degeneracy,

for example in a sample subjected to a magnetic or pseudomagnetic field, provided that the Fermi energy is chosen appropriately. Strain-induced pseudomagnetic fields have been suggested to lift the degeneracy of the K and K' points by 100 meV.^{27,28}

We conclude by pointing out the differences between coherent current control in graphene and in conventional semiconductors such as GaAs. In two-color CC experiments in gapped semiconductors, the fields are typically chosen so that the semiconducting bandgap E_g lies between $\hbar\omega < E_g < 2\hbar\omega$. Thus, one-photon absorption at the fundamental frequency is energetically forbidden. However, since the band dispersions of graphene and bilayer graphene are gapless, for a clean, unbiased sample there is a nonzero joint density of states down to zero frequency and one-photon absorption is always present. This raises an issue for two-color CC experiments where the usual best practice is to have balanced absorption between the first-order process at 2ω and the second-order process at ω . To achieve this, the fundamental beam is given most of the power. If this beam is absorbed in the linear regime, it can potentially flood the sample with carriers that are not taking part in the quantum interference. We note however that this has not led to difficulties in observing the coherent current control in multilayer epitaxial graphene.¹³

The opening of a sufficiently large gap in the band dispersion of graphene would completely eliminate one-photon

absorption at ω . The weak spin-orbit coupling offers only a very small gap that has been calculated to be on the μeV scale for graphene^{29,30} and bilayer graphene,³¹ while gaps induced by the substrate^{15,32,33} or by confinement^{34,35} (in certain nanoribbon geometries, similar to the way carbon nanotubes can acquire a gap) are typically tens of meV. Most interestingly, in bilayer graphene gap opening can also occur due to z -axis asymmetry between the two layers, which can be field induced.³⁶ Field-induced gaps are tunable up to hundreds of meV.

The problem of linear absorption of the fundamental could also be circumvented by a nonzero Fermi energy E_F , taking advantage of Pauli blocking to prevent one-photon absorption at ω . With the relation $\hbar\omega/2 < |E_F| < \hbar\omega$, one effectively has the same condition as typical gapped semiconductors. This offers even more tunability since the Fermi energy can be gate controlled, and could lead to novel electro-optical devices making use of coherent current control.

ACKNOWLEDGMENTS

This work was supported by FQRNT, by DFG under Projects No. SFB 767 and No. FOR 912, and by CAP and NSERC. The authors acknowledge useful discussions with Dong Sun and Ted Norris.

¹K. S. Novoselov, A. K. Geim, S. V. Morozov, D. Jiang, Y. Zhang, S. V. Dubonos, I. V. Grigorieva, and A. A. Firsov, *Science* **306**, 666 (2004).

²K. S. Novoselov, D. Jiang, F. Schedin, T. J. Booth, V. V. Khotkevich, S. V. Morozov, and A. K. Geim, *Proc. Nat. Acad. Sci. USA* **102**, 10451 (2005).

³K. S. Novoselov, A. K. Geim, S. V. Morozov, D. Jiang, M. I. Katsnelson, I. V. Grigorieva, S. V. Dubonos, and A. A. Firsov, *Nature* **438**, 197 (2005).

⁴E. McCann and V. I. Fal'ko, *Phys. Rev. Lett.* **96**, 086805 (2006).

⁵A. H. Castro Neto, F. Guinea, N. M. R. Peres, K. S. Novoselov, and A. K. Geim, *Rev. Mod. Phys.* **81**, 109 (2009).

⁶R. R. Nair, P. Blake, A. N. Grigorenko, K. S. Novoselov, T. J. Booth, T. Stauber, N. M. R. Peres, and A. K. Geim, *Science* **320**, 1308 (2008).

⁷K. S. Novoselov, E. McCann, S. V. Morozov, V. I. Fal'ko, M. I. Katsnelson, U. Zeitler, D. Jiang, F. Schedin, and A. K. Geim, *Nature Phys.* **2**, 177 (2006).

⁸M. I. Katsnelson, *Eur. Phys. J. B* **52**, 151 (2006).

⁹S. V. Morozov, K. S. Novoselov, M. I. Katsnelson, F. Schedin, D. C. Elias, J. A. Jaszczak, and A. K. Geim, *Phys. Rev. Lett.* **100**, 016602 (2008).

¹⁰H. Rabitz, in *Encyclopedia of Modern Optics*, edited by B. D. Guenther (Elsevier, Oxford, 2005), pp. 123–133; R. J. Lewis, *Encyclopedia of Modern Optics*, edited by B. D. Guenther (Elsevier, Oxford, 2005), pp. 133–137; H. M. van Driel and J. E. Sipe, *Encyclopedia of Modern Optics*, edited by B. D. Guenther (Elsevier, Oxford, 2005), pp. 137–143.

¹¹R. Atanasov, A. Haché, J. L. P. Hughes, H. M. van Driel, and J. E. Sipe, *Phys. Rev. Lett.* **76**, 1703 (1996).

¹²E. J. Mele, P. Král, and D. Tománek, *Phys. Rev. B* **61**, 7669 (2000).

¹³D. Sun, C. Divin, J. Rioux, J. E. Sipe, C. Berger, W. A. de Heer, P. N. First, and Th. B. Norris, *Nano Lett.* **10**, 1293 (2010).

¹⁴R. W. Newson, J.-M. Ménard, C. Sames, M. Betz, and H. M. van Driel, *Nano Lett.* **8**, 1586 (2008).

¹⁵E. J. Nicol and J. P. Carbotte, *Phys. Rev. B* **77**, 155409 (2008).

¹⁶H. M. van Driel and J. E. Sipe, in *Ultrafast Phenomena in Semiconductors*, edited by K.-T. Tsen (Springer-Verlag, Berlin, 2000), Chap. 5, pp. 261–306.

¹⁷Other nonzero components of the isotropic model are $\xi^{xyxy} = \xi^{xyyx} = \frac{1}{2}\xi^{xxxx}(1 - \delta)$, and those obtained by $x \leftrightarrow y$ permutations, omitted throughout for simplicity; see D. C. Hutchings and B. S. Wherrett, *Opt. Mater.* **3**, 53 (1994).

¹⁸V. P. Gusynin, S. G. Sharapov, and J. P. Carbotte, *Phys. Rev. Lett.* **96**, 256802 (2006).

¹⁹Looking at how the interference term in the carrier injection transforms under the action of inversion symmetry, one gets $\dot{n}_I = \xi_I^{abc}(\omega)E^{a*}(\omega)E^{b*}(\omega)E^c(2\omega) + \text{c.c.} \rightarrow \dot{n}_I = -\xi_I^{abc}(\omega)E^{a*}(\omega)E^{b*}(\omega)E^c(2\omega) + \text{c.c.}$, which imposes $\xi_I = 0$.

²⁰A. Najmaie, R. D. R. Bhat, and J. E. Sipe, *Phys. Rev. B* **68**, 165348 (2003).

²¹R. D. R. Bhat and J. E. Sipe, e-print [arXiv:cond-mat/0601277](https://arxiv.org/abs/cond-mat/0601277) (unpublished).

²²D. S. L. Abergel and V. I. Fal'ko, *Phys. Rev. B* **75**, 155430 (2007).

²³W. A. de Heer, C. Berger, X. Wu, P. N. First, E. H. Conrad, X. Li, T. Li, M. Sprinkle, J. Hass, M. L. Sadowski, M. Potemski, and G. Martinez, *Solid State Commun.* **143**, 92 (2007).

²⁴H. Min and A. H. MacDonald, *Phys. Rev. Lett.* **103**, 067402 (2009).

²⁵T. Stauber, N. M. R. Peres, and A. K. Geim, *Phys. Rev. B* **78**, 085432 (2008).

- ²⁶M. Koshino and T. Ando, *Phys. Rev. B* **77**, 115313 (2008).
- ²⁷F. Guinea, M. I. Katsnelson, and A. K. Geim, *Nature Phys.* **6**, 30 (2010).
- ²⁸F. Guinea, A. K. Geim, M. I. Katsnelson, and K. S. Novoselov, *Phys. Rev. B* **81**, 035408 (2010).
- ²⁹H. Min, J. E. Hill, N. A. Sinitsyn, B. R. Sahu, L. Kleinman, and A. H. MacDonald, *Phys. Rev. B* **74**, 165310 (2006).
- ³⁰M. Gmitra, S. Konschuh, C. Ertler, C. Ambrosch-Draxl, and J. Fabian, *Phys. Rev. B* **80**, 235431 (2009).
- ³¹F. Guinea, *New J. Phys.* **12**, 083063 (2010).
- ³²E. McCann, *Phys. Rev. B* **74**, 161403 (2006).
- ³³C. Enderlein, Y. S. Kim, A. Bostwick, E. Rotenberg, and K. Horn, *New J. Phys.* **12**, 033014 (2010).
- ³⁴L. Brey and H. A. Fertig, *Phys. Rev. B* **73**, 235411 (2006).
- ³⁵M. Y. Han, B. Özyilmaz, Y. Zhang, and P. Kim, *Phys. Rev. Lett.* **98**, 206805 (2007).
- ³⁶Y. Guo, W. Guo, and C. Chen, *Appl. Phys. Lett.* **92**, 243101 (2008).